ACSNANO

www.acsnano.org

ARTICLE

Ultrafast Ambient-Air Exsolution on Metal Oxide via Momentary Photothermal Effect

Euichul Shin, Dong-Ha Kim, Jun-Hwe Cha, Seolwon Yun, Hamin Shin, Jaewan Ahn, Ji-Soo Jang, Jong Won Baek, Chungseong Park, Jaehyun Ko, Seyeon Park, Sung-Yool Choi,* and Il-Doo Kim*

Cite This: *ACS Nano* 2022, 16, 18133–18142

Read Online

ACCESS | Metrics & More | Article Recommendations | Supporting Information

ABSTRACT: The process of exsolution for the synthesis of strongly anchored metal nanoparticles (NPs) on host oxide lattices has been proposed as a promising strategy for designing robust catalyst-support composite systems. However, because conventional exsolution processes occur in harsh reducing environments at high temperatures for long periods of time, the choice of support materials and dopant metals are limited to those with inherently high thermal and chemical stability. Herein, we report the exsolution of a series of noble metal catalysts (Pt, Rh, and Ir) from metal oxide nanofibers (WO_3 NFs) supports in an entirely ambient environment induced by intense pulsed light (IPL)-derived momentary photothermal treatment (>1000 °C). Since the exsolution process spans an extremely short period of time (<20 ms), unwanted structural artifacts such as decreased surface area and phase transition of the support materials are effectively suppressed. At the same time, exsolved NPs (<5 nm) with uniform size distributions could successfully be formed. To prove the practical utility of exsolved catalytic NPs functionalized on WO_3 NFs, the chemiresistive gas sensing characteristics of exsolved Pt-decorated WO_3 NFs were analyzed, exhibiting high durability (>200 cyclic exposures), enhanced response (R_{air}/R_{gas} > 800 @ 1 ppm/350 °C), and selectivity toward H_2S target gas. Altogether, we successfully demonstrated that ultrafast exsolution within a few milliseconds could be induced in ambient conditions using the IPL-derived momentary photothermal treatment and contributed to expanding the practical viability of the exsolution-based synthetic approaches for the production of highly stable catalyst systems.

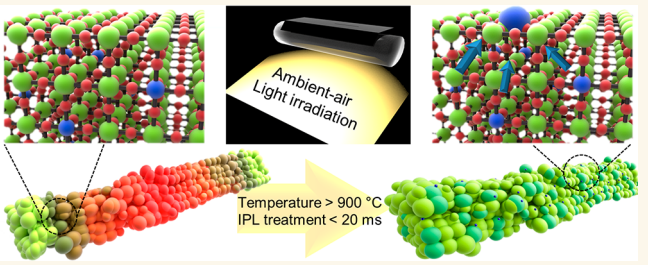

KEYWORDS: *ambient-air process, exsolution, intense pulsed light process, momentary photothermal effect, tungsten oxide nanofibers*

INTRODUCTION

Heterogeneous catalysts, particularly those based on supported metal nanoparticles (NPs), play an important role in promoting various industrially relevant chemical reactions for the production of high-value-added products. It is widely understood that the catalytic performance depends on their surface morphology and composition, which therefore must be carefully engineered for producing practically viable heterogeneous catalysts.[1,2] In addition to their initial morphology and composition, the catalyst NPs must also remain stable against deformation and/or agglomeration over repeated reaction cycles under typically harsh chemical environments. In this regard, a recently introduced synthetic technique based on the phenomenon of exsolution has shown much promise for producing catalysts with excellent robustness and high reactivity. The exsolution process involves the nucleation and growth of catalyst metal NPs on the surface of metal oxide supports driven by reductive heat treatment of the support material doped with the catalyst metal ions, which results in the formation of socketed catalyst NP structures that induce reciprocal strain and smooth interfaces.[3,4] Based on the outstanding catalytic properties of exsolved metal NPs, they have been utilized in various applications, including oxidation catalysts, gas sensors, and solid oxide fuel cells.[5−7]

However, conventional exsolution techniques face several challenges from the fact that the support materials must endure harsh conditions, such as elevated temperatures (>500−1000 °C), highly reducing atmospheres that impose safety hazards (e.g., H_2), and perhaps most importantly, long process times up to 24 h (Table S1). Therefore, materials that are vulnerable to deformation and phase change in a strongly reducing environment cannot be utilized as host materials for the

Received: May 25, 2022
Accepted: September 8, 2022
Published: September 15, 2022

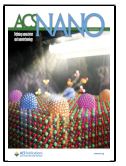

https://doi.org/10.1021/acsnano.2c05128
ACS Nano 2022, 16, 18133−18142

exsolution process to reliably generate exsolved catalyst NPs, limiting the versatility of the exsolution-based approach. As such, it is worth the effort to explore alternative synthetic routes that can be used to prepare exsolved NPs with a wide variety of host materials/exsolute element combinations. In this regard, Myung et al. demonstrated an electrochemical reduction route to create exsolved NPs from $La_{0.43}Ca_{0.37}Ni_{0.06}Ti_{0.94}O_3$ by applying an external bias to induce a pO_2 gradient across the material system.[8] It was hypothesized that the sharp gradient acted as the driving force for rapid exsolution (i.e., ~100 s in 50% H_2O/N_2 gases). In addition, Tan et al. synthesized exsolved Ni NPs from a ceria matrix codoped with Ni and Gd ($Gd_{2-x}Ni_xCe_{0.8}O_{2-\delta}$) at extremely high temperatures (>1000 °C) in ambient air, which decreased the oxygen content in the metal oxide.[9] In this case, the elevated temperature induces the diffusion of oxygen species in bulk to the surface, even without the presence of reducing gases. Moreover, Jang et al. demonstrated the low-temperature (<300 °C) exsolution method using Ir-doped tungsten oxide nanosheet as a starting material.[10] In particular, Ir doping could trigger a phase transition in the host tungsten oxide nanosheet matrix to enhance their resilience against reductive degradation, which facilitates the formation of exsolved Ir NPs at the surface of the oxide upon reductive heat treatment without heavily damaging the oxide support.

Although the aforementioned strategies (i.e., fast exsolution, ambient-air exsolution, low-temperature exsolution assisted by dopant-induced phase change) have provided viable routes for achieving exsolution for specific material systems, several critical limitations still remain for extending the exsolution-based synthesis to other combinations of host materials and dopant metals, particularly for host oxides that are vulnerable to damage from chemical reduction. A straightforward approach to prevent the loss of surface area and disruptions in the host oxide lattice is required to significantly reduce the overall processing time, which can be achieved if we could rapidly induce the appropriate experimental conditions for exsolution. Notably, several strategies for the rapid synthesis of nanostructures based on various momentary heat-treatment techniques have been demonstrated in the literature, such as those utilizing joule heating, microwave heating, laser annealing, and intense pulsed light (IPL) treatment.[11−15] While the first two techniques are limited to small processing areas (laser annealing), conductive substrates (joule heating), or relatively long processing times in the minute-scale (microwave heating), the IPL-based strategy can be used to induce rapid thermal shocks of temperatures up to thousands of °C within a few milliseconds across a large area, making IPL the most suitable synthetic method for reliable and large-scale synthesis. The heating mechanism of IPL is based on the photothermal effect, which refers to the generation of heat in the target material when it is irradiated by photons with an energy that is larger than its bandgap. Therefore, the IPL method could be applied to a diverse selection of oxide supports as long as they exhibit appropriate photothermal efficiencies, and it has also been reported that the photothermal efficiency of various oxide materials could be enhanced through IPL treatment as an additional measure.[15] Overall, the IPL-derived momentary photothermal (hereafter, IPL-MP) treatment should be able to induce high temperatures that are sufficient to exsolve nanoscale particles within a few milliseconds in ambient air conditions while ensuring minimal damage to the oxide support.

Here, we demonstrate the ambient-air exsolution process using IPL-MP treatment as a practically viable exsolution-based synthesis platform. In a standard protocol, WO_3 nanofibers (NFs) doped with various noble metals (hereafter, M-WO_3 NFs, where M denotes metal dopant) were first prepared via electrospinning and subsequent oxidative calcination processes. Then, by applying IPL irradiation, sub-10 nm metal NPs were formed on the surface of WO_3 NFs with a uniform distribution (IPL_exsolved M-WO_3 NFs), indicative of the exsolution of the noble metal species from the oxide matrix. The IPL irradiation method induces little to no phase transition in the host oxides owing to its ultrafast processing time (<20 ms).[16] In addition, we investigated the practical feasibility of the IPL-generated exsolved NP catalysts by evaluating the chemiresistive gas sensing performances of IPL_exsolved M-WO_3 NFs. As a result, IPL_exsolved Pt-WO_3 NFs showed one of the highest recorded H_2S sensing responses (R_{air}/R_{gas} > 800 @ 1 ppm/350 °C) with excellent durability (>200 cyclic exposures) when compared with the state-of-the-art chemiresistors based on semiconducting metal oxides. Notably, the ambient-air IPL-induced exsolution method could be extended to many different types of oxides, including ternary oxides (e.g., $LaFeO_3$) that have already been widely studied in the field of exsolution.

RESULTS AND DISCUSSION

Herein, we selected tungsten oxide (WO_3) as the model system to study the feasibility of exsolution triggered by the IPL-MP process. Tungsten oxides have a particularly low activation energy for exsolution because they exhibit (i) significant phase transitions upon doping[10] as well as (ii) high photothermal efficiencies due to localized surface plasmon resonance effects at their oxygen-deficient sites.[17] To prepare the metal-doped WO_3 NFs as the support material, we first prepared an aqueous electrospinning solution containing ammonium metatungstate hydrate ($[(NH_3)_6H_2W_{12}O_{40}\cdot xH_2O]$) and polyvinylpyrrolidone (PVP), to which equimolar portions of chloroplatinic acid hexahydrate ($H_2PtCl_6\cdot 6H_2O$), rhodium chloride hydrate ($RhCl_3\cdot xH_2O$), or iridium chloride hydrate ($IrCl_3\cdot xH_2O$) were added as the noble metal precursors. The noble metals were easily incorporated within metal oxide lattice as the precursor-loaded electrospun NFs were calcined in ambient air.[18] Bright-field transmission electron microscopy (TEM), high-angle annular dark-field scanning transmission electron microscopy (HAADF-STEM), and energy-dispersive X-ray spectroscopy (EDS) mapping images confirmed that W, O, and especially the dopant metals were present in appreciable amounts in calcined M-WO_3 NFs (Figures S1−S3, Supporting Information), the noble metals contained 0.04 at%, 0.3 at%, 0.3 at% of Pt, Rh, and Ir, respectively. The resulting metal-doped WO_3 NFs were used as the substrate for IPL-MP treatments to induce exsolution in an ambient environment.

We characterized how efficiently the noble metals were doped in the WO_3 NFs matrix by monitoring the changes in their crystal lattice structure as a function of the doping amounts of each element. Specifically, powder X-ray diffraction patterns (PXRD) were collected for each WO_3 sample and doped with different amounts of each noble metal (i.e., Pt, Rh, and Ir). The crystal structures of the WO_3 and M-WO_3 NFs were assigned to that of monoclinic WO_3 based on the observed characteristic XRD peaks (JCPDS no. 43-1035) (Figures S4a and S5a−c). Notably, for all types of metals, we

https://doi.org/10.1021/acsnano.2c05128
ACS Nano 2022, 16, 18133−18142

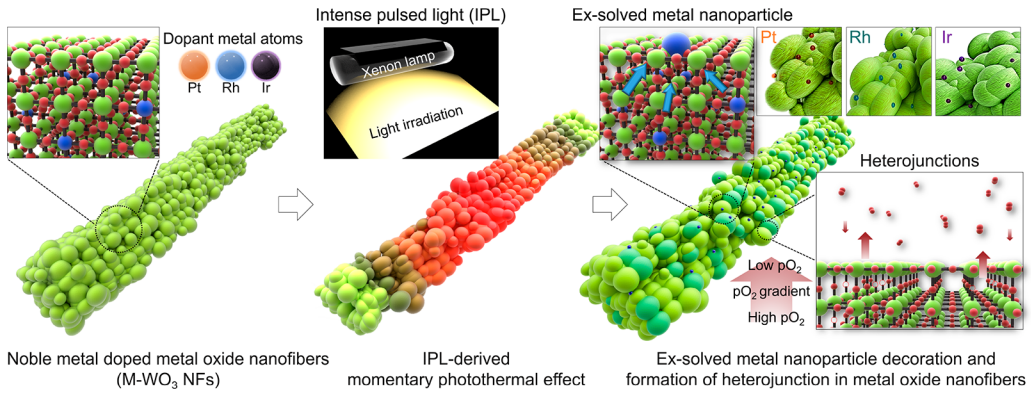

Figure 1. Schematic diagram of exsolved noble metals decoration on WO_3 NFs via IPL derived momentary photothermal treatment with a mechanism of heterojunctions and exsolution formation. In the atomic diagram, red, green, and blue spheres in tungsten oxide are oxygen, tungsten, and dopant atoms, respectively.

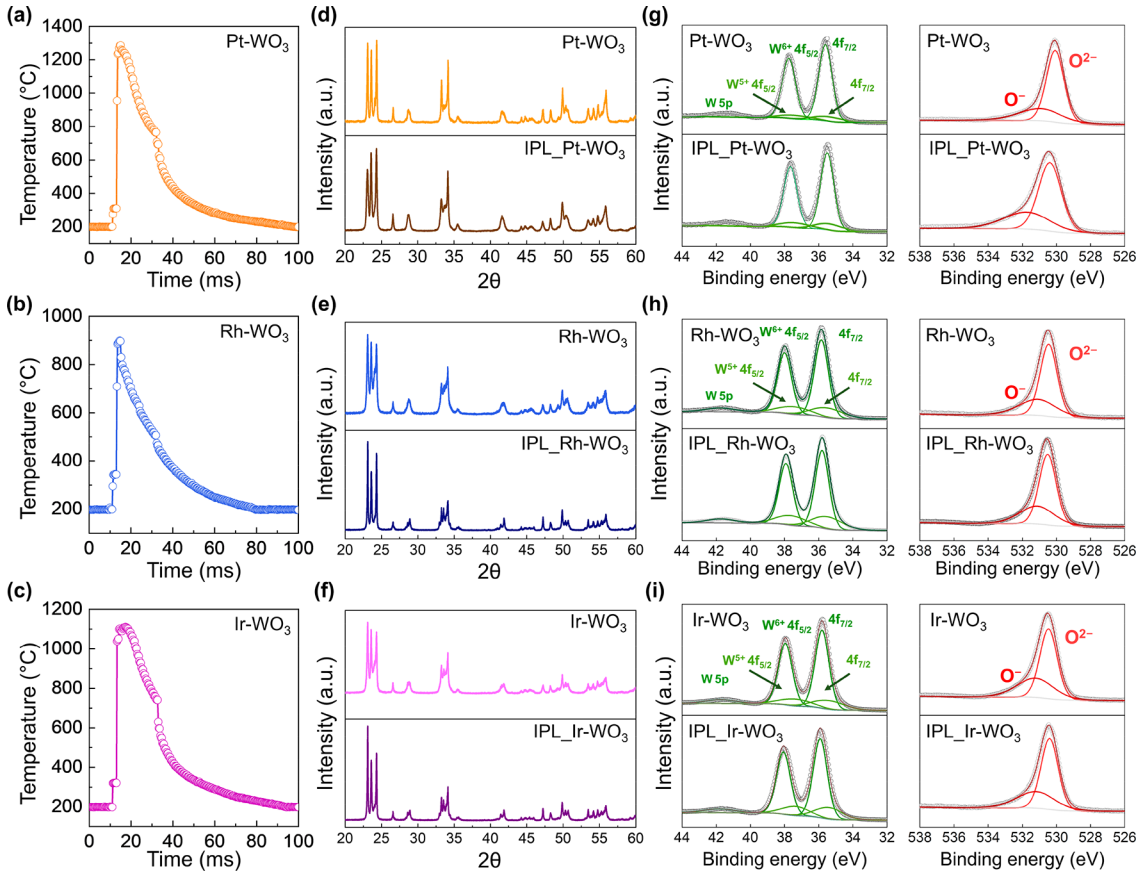

Figure 2. (a–c) Temperature–time curve of M-WO_3 NFs under intensive irradiations (19–20 J/cm^2). (d–f) The XRD analysis of M-WO_3 and IPL_M-WO_3 NFs and (g–i) ex situ XPS analysis of M-WO_3 NFs before and after IPL process in the vicinity of W 4f peaks and O 1s peaks.

found that the PXRD patterns only show minute changes as a function of dopant concentration with no indication of metallic peaks, suggesting that there is no significant phase separation of the dopant metals from the WO_3 lattice. Furthermore, by calculating the average volume of each M-doped WO_3 NFs based on the positions of monoclinic WO_3 peaks corresponding to (200), (020), and (002),[19] we found that the lattices exhibit slight volume contractions as the doping level increased, regardless of the type of dopant metal (Figure S5d–f). This observation indicates the Pt, Rh, and Ir atoms replace the W sites in the WO_3 lattice by substitution. Also, the solubility of Pt, Rh, Ir in monoclinic WO_3 NFs can be estimated to be at the point where the change in lattice volume per dopant concentration begins to diminish sharply, which was around 0.1, 0.6, 1 at%, respectively. With Pt as a case study, we found evidence of aggregates Pt NPs formed on the surface of WO_3 when doped with 0.08 at% and 0.24 at% of Pt (Figure S6), while Pt NPs could not be found on WO_3 doped with <0.08 at%, even after a thorough manual search. In order to avoid phase separation of the dopant metal before the photothermal heating, we prepared M-WO_3 NFs with reasonable amounts of metal dopants (0.04 at% Pt, 0.3 at%

https://doi.org/10.1021/acsnano.2c05128
ACS Nano 2022, 16, 18133–18142

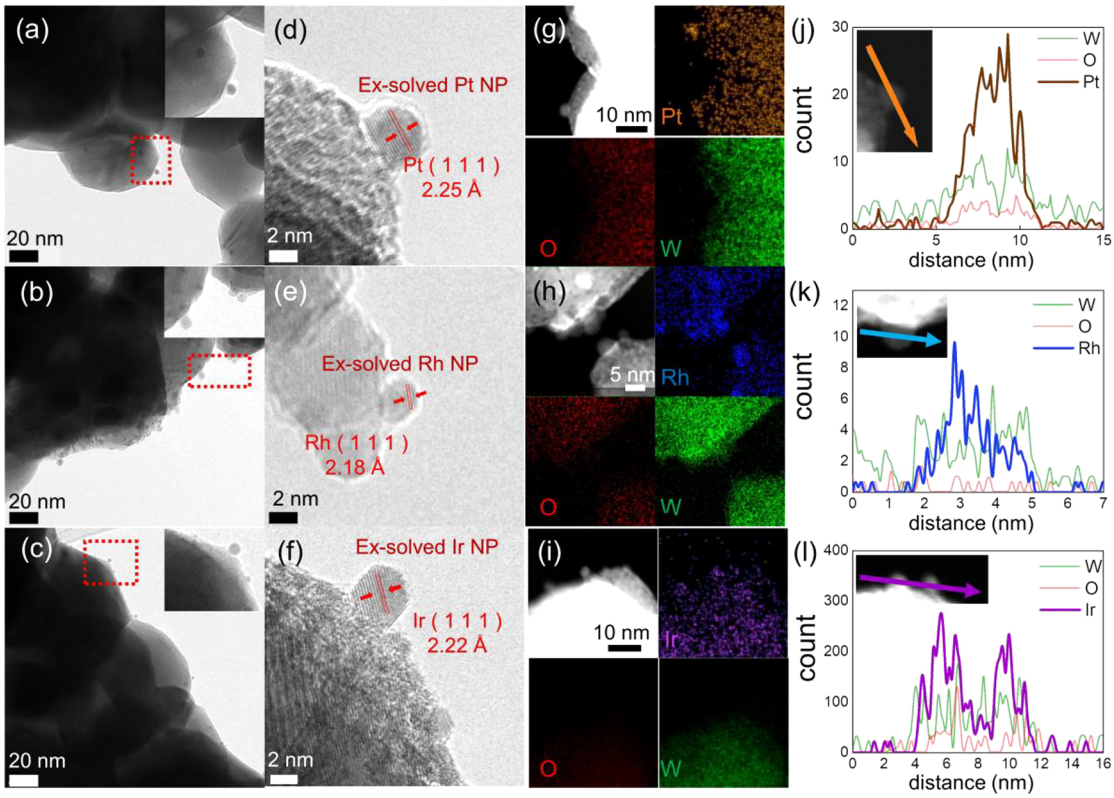

Figure 3. TEM images of (a) IPL1_exsolved Pt-WO_3 NFs, (b) IPL10_exsolved Rh-WO_3 NFs, and (c) IPL1_exsolved Ir-WO_3 NFs and their HRTEM images (d–f), respectively. EDS element mapping of W, O, and (g–i) Pt, Rh, Ir. The data plost of line scan profile of (j–l) exsolved Pt, Rh, and Ir NPs.

Rh, and 0.1/0.3 at% Ir, respectively), such that the formation of exsolved NPs could be explicitly attributed to the IPL-MP treatment.

The resulting intensive photothermal heat provides sufficient energy to overcome the activation energy barrier against exsolution, as illustrated in the schematic diagram for the proposed reaction mechanisms of the IPL-MP treatment (Figure 1). As the WO_3 NFs and M-WO_3 NFs were irradiated by a pulse of intensive light with photon energies exceeding the bandgap of WO_3 (2.4–2.8 eV),[20] the temperature in the Pt, Rh, and Ir-doped WO_3 NFs spiked with ultrafast heating rates of about 4.63, 3.33, and 4.45 × 10^5 K s^{-1} (Figure 2a–c). Notably, the heating rates and maximum temperatures varied as a function of the type of dopant as well as their concentration. Specifically, we hypothesize that the elevated temperatures (>1000 °C) induced in the host materials by momentary photothermal treatment provide a sufficient driving force for the release of oxygen atoms from the oxide lattice due to the formation of an oxygen concentration gradient across the interface between the oxide lattice and ambient air, serving as a quasi-reducing environment in the high-temperature transient.[9,15,16] As a result, the IPL-treated samples would undergo a partial reduction of the oxide lattice near the surface for the formation of several WO_{3-x}/WO_3 heterojunctions while also forming exsolved metal NPs, together with facilitating a higher catalytic activity and chemiresistive sensitivity. By controlling the IPL irradiation conditions, such as the number of shots and duration of irradiation times, the size and distribution of NPs could be adjusted for optimizing the catalytic behavior for various applications.

In one aspect, the IPL-MP treatment enhanced the crystallinity of the WO_3 matrix for each of the M-WO_3 NFs (Figure S4a, Figure 2d–f). In fact, the average crystalline sizes of WO_3, Pt-WO_3, Rh-WO_3, and Ir-WO_3 NFs upon single-shot IPL-MP treatment, as calculated using the Scherrer formula, showed an increase from 30 to 40, 32 to 54, 35 to 60, and 37 to 57 nm, respectively (Methods section for details). Although the photothermal temperature almost reached the melting temperature of WO_3 (<1400 °C), the fibrous nanostructures were well-maintained because of the extremely short heat treatment (<20 ms), highlighting one major advantage of the IPL-MP treatment method (Figures S7 and S8). Moreover, the monoclinic phase of WO_3 was also mostly retained upon photothermal heating, as shown in Figure 2d–f and Figure S4a. For reference, the thermodynamically stable crystal structure of WO_3 at above 740 °C is in the tetragonal phase.[20] Additionally, these results showed that the IPL-MP treatment could induce high temperatures without severe deformations in the phase and structure of host materials with a relatively low thermal budget. Additionally, the fibrous structures and the monoclinic phase could be preserved without deformation and phase transitions even after 10 consecutive irradiations, demonstrating the excellent reliability of the IPL-MP treatment (Figure S9).

Despite the fact that the IPL-MP treatment did not affect the bulk crystal structure, we found that the surface chemistry of the WO_3 lattice was slightly modified, as observed from ex situ X-ray photoelectron spectroscopy (XPS) measurements. For each sample, we calculated the peak area ratio of tungsten and oxygen oxidation states, respectively (i.e., W^{5+}/W^{6+}, O^-/O^{2-}), the increase in which indicates partial chemical reduction.

https://doi.org/10.1021/acsnano.2c05128
ACS Nano 2022, 16, 18133–18142

Across all samples, two pairs of characteristic peaks could be identified in the W 4f region, i.e., $4f_{5/2}$ and $4f_{7/2}$, corresponding to the binding energies of W^{6+} (37.8 and 35.6 eV) and W^{5+} (37.6 and 35.4 eV), respectively.[21] Oxygen 1s peaks were located at 530.2 eV for O^{2-} (lattice oxygen species) and 531.0 eV for O^- (chemisorbed oxygen species).[22] Figure 2g–i and Figure S2b show that, after IPL-MP treatments, the peak area ratios for tungsten (W^{5+}/W^{6+}) in pristine WO_3 were increased by 53%, while those in M-WO_3 NFs were increased by relatively smaller amounts such as 20% (Pt), 21% (Rh), or 12% (Ir) (Table S2). Likewise, for oxygen (O^-/O^{2-}), the peak area ratio increased in pristine WO_3 by 46%, while it only increased by 23% (Pt), 6% (Rh), or 11% (Ir) for the metal-doped WO_3 NFs (Table S3). This difference can be attributed to the formation of additional heterojunctions on the NFs surface due to the formation of noble metal NPs by IPL-induced exsolution. Moreover, Figure S10 exhibits XPS analyses of Pt 4f, Rh 3d, and Ir 4f for Pt-, Rh-, and Ir-WO_3 NFs before (a–c) and after (d–f) IPL treatment. After the IPL process, the metallic statse of Rh and Ir were confirmed at 307.0 and 61.13 eV, which indicated $3d_{5/2}$ of Rh^0 and $4f_{7/2}$ of Ir^0, respectively.[23] However, we did not find any peaks of Pt in Pt-WO_3 NFs before and after the IPL process since the amounts of platinum were contained at 0.04 at% compared to tungsten, which was lower than the detection limit of spectroscopy. Although the XPS analysis did not confirm the existence of exsolved Pt NPs, it was indirectly confirmed by the improvement of the density of adsorbed oxygen species. The improvement of the amount of chemisorbed oxygen (O^-) exhibited the existence of the exsolved Pt NPs, which induce spillover from oxygen (O_2) to chemisorbed oxygens (Figure 2g and Figure S11). We then performed electron microscopy to characterize the exsolved NPs obtained by IPL-MP treatment of M-WO_3 NFs. Figure 3a–c shows the TEM images of exsolved NPs on the surface of IPL-treated Pt-WO_3 (0.04 at% Pt), Rh-WO_3 (0.3 at% Rh), and Ir-WO_3 (0.1 at% Ir) NFs, for which all samples received a single-shot IPL-MP treatment with the exception of the Rh-containing sample that received 10 consecutive treatments. Additional TEM images can be found in Figure S12 for reference. The high-resolution TEM (HRTEM) images of the exsolved NPs clearly revealed the (111) lattice fringes of Pt, Rh, and Ir corresponding to the measured interplanar spacing of 2.25, 2.18, and 2.22 Å, respectively (Figure 3d–f). Also, the average radii of exsolved Pt, Rh, and Ir NPs were measured to be 2–3 nm. Moreover, the EDS mapping (Figure 3g–i) and line scan profiles (Figure 3j–l) reveal uniform distributions of Pt, Rh, and Ir elements within the respective exsolved NPs, and that the exsolved NPs are well-distributed on the surface of WO_3 NFs. Altogether, we successfully demonstrated that the IPL-MP treatment could be used to synthesize exsolved NPs of various metals on the surface of WO_3 NFs in ambient-air conditions with a low thermal budget.

We evaluated the morphology of exsolved Pt-WO_3 NFs obtained by IPL-MP treatment against the Pt-WO_3 NFs prepared by conventional reductive heat treatment at 500 °C for 1 h (4% H_2/Ar atmosphere). In general, thermal annealing of reducible metal oxides such as WO_3 by convective heat transfer in a high temperature and reducing atmosphere for extended periods of time could degrade the extrinsic properties of the host material such as the specific surface area and induce excessive phase transition and/or reduction of the host materials. Although the furnace-treated Pt-WO_3 NFs clearly show exsolved Pt NPs (5–6 nm) scattered on the surface of WO_3, the PXRD data confirmed that WO_3 had transitioned to $WO_{2.9}$ and WO_2 upon furnace treatment (Figure S13), as expected.

To demonstrate the general applicability of the IPL-derived ambient-air exsolution strategy toward a variety of host materials, we further attempted the IPL-based exsolution of metal NPs from a $LaFeO_3$ (LFO) matrix, a typical perovskite NF material. LFO has widely been studied for exsolution because of its excellent thermal/chemical stability as well as the high photothermal efficiency in visible light (bandgap ≈2.6 eV) that makes it suitable for IPL irradiation.[24−27] Indeed, we found that the Pt-LFO and Rh-LFO NFs exhibit sharp increases in temperature upon IPL irradiation, similar to WO_3 NFs, up to nearly 800 and 1200 °C, respectively. The exsolved Pt and Rh NPs were successfully synthesized with uniform size distributions (<5 nm) on the surface of LFO NFs (Figure S14). Therefore, we could conclude that the IPL-MP treatment is applicable even for reducible oxides and complex multicomponent oxides, which greatly helps to extend the possible metal-support combinations of exsolved NP catalyst systems as designed catalysts tailored to specific applications.

Since the semiconducting metal oxide-based chemiresistive gas sensor tests are operated at high temperatures (>200 °C) and, according to applications (e.g., breath analysis), need additional humidity atmospheres, the decorated metal NPs must also resist aggregation and/or agglomeration during repeated reactions in such severe chemical conditions (i.e., high temperature and humidity).[28] Recent studies on the exsolution-based catalyst synthetic methods have shown promising features to prepare highly robust and reactive catalysts on the surface of metal oxide. However, the support materials must withstand high temperatures under a reducing atmosphere for a prolonged synthetic times to synthesize the exsolved metal NPs (Table S1). Such severe synthetic conditions spontaneously induce a decrease of active sites and unwanted phase transitions. In this regard, the IPL-based strategy could be a breakthrough strategy to overcome such limitations by inducing rapid heat treatment up to >1000 °C in milliseconds time scale that is sufficient to exsolve NPs on metal oxide surface while minimizing thermal damage to the support materials. The main sensing mechanism of semiconducting metal oxide-based chemiresistive gas sensors relies on dominant surface reactions between gas analytes and chemisorbed oxygen species (O^-). In particular, the decoration of catalytic NPs on the surface of semiconducting metal oxide-based gas sensors could greatly enhance the sensing performance via the so-called spillover effect, but an excessive amount of catalyst could either be agglomerated or block the surface active sites of metal oxides to induce deterioration in the overall sensing performances. In fact, it is well-known that introducing only a trace amount (<0.1 at%) of noble metal catalysts on metal oxide supports could dramatically improve the gas sensing properties.[15] Therefore, we believe that the low concentration (<1 at%) of catalysts was suitable to enhance the gas sensing performances in our system. To demonstrate the practical feasibility of IPL_M-WO_3 NFs containing exsolved NPs, we evaluated their chemiresistive gas sensing properties. The gas sensing tests were conducted toward various breath biomarker gas molecules, including hydrogen sulfide (H_2S), dimethylsulfide (C_2H_6S), acetone (C_3H_6O), ethanol (C_2H_5OH), and ammonia (NH_3). Of these gases, in particular, H_2S is an important biomarker for the diagnosis of halitosis when detected from exhaled breath; thus, the development of a

https://doi.org/10.1021/acsnano.2c05128
ACS Nano 2022, 16, 18133−18142

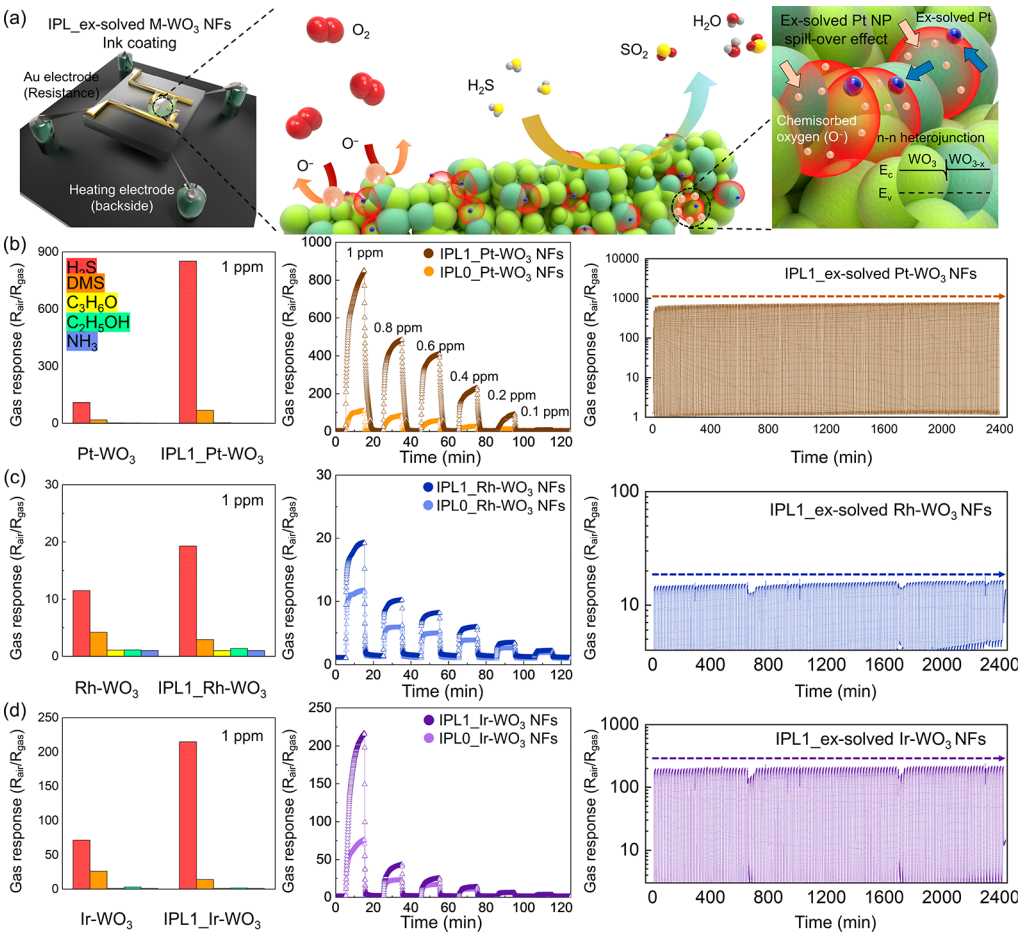

Figure 4. (a) Schematic illustrations of the gas sensor device system and sensing mechanism of IPL_exsolved M-WO_3 NFs. (b–d) Selective gas sensing characteristics, hydrogen sulfide gas sensing results from 1 to 100 ppb concentrations, and long-term durability test toward 1 ppm of H_2S of IPL_exsolved M-WO_3 NFs.

practical H_2S sensor with a low detection limit of at least parts per billion in concentration as well as selectivity against high humidity and many interfering gases is in high demand.[28,29] As illustrated in Figure 4a, the exsolved Pt NPs on the surface of WO_3 contribute to enhancing the sensing performance of WO_3 via the spillover effect, which accelerates the decomposition of oxygen gas (O_2) into chemisorbed oxygen (O^-). The exsolved Pt NPs on the WO_3 matrix, therefore, should effectively serve this role to facilitate gas decomposition to enhance sensitivity and selectivity in chemiresistive sensors.[30] The spillover effect is evident considering that, for the case study of Pt-WO_3, the XPS area ratio between the chemisorbed oxygen species (O^-) and the lattice oxygen species (O^{2-}) was enhanced by a factor of 2 after applying the IPL-MP treatment, indicating that more O^- species could be formed in the presence of exsolved Pt NPs. Moreover, the consecutive IPL-MP treatments on Pt-WO_3 NFs increased the number of exsolved Pt NPs, which stimulated the absorption of oxygen species (Figure S11). As H_2S reacts with the chemisorbed oxygen, it is decomposed to SO_2 by the following reaction: $H_2S + 3O^- \rightarrow SO_2 + H_2O + 3e^-$.[30] Moreover, the heterojunction across the interface between WO_3 (work function ≈6.5 eV) and WO_{3-x} (work function ≈6.35 eV), which formed as a result of the IPL-induced surface modulation, promotes electron transfer from WO_{3-x} to WO_3, which enhances the gas response due to band bending and expansion of the electron depletion layer.[31,32] The base resistance of pristine WO_3 NFs was increased more than twice, which derived from the formation of heterojunctions between WO_3 and WO_{3-x}. Therefore, the gas response toward H_2S was enhanced ≈30% after IPL-treatment (Figure S15). Altogether, the exsolved catalyst-decorated WO_3 NFs prepared by IPL-MP are an excellent material for the selective and quantitative detection of H_2S.

Based on our analysis, there are sufficient grounds to conclude that IPL-treated M-WO_3 NFs should be superior to those prepared by conventional exsolution. To confirm that this is the case, we comparatively evaluated the sensing performances of different kinds of M-WO_3 NFs, furnace-treated M-WO_3 NFs, and IPL-treated M-WO_3 NFs. For each material, prototype sensors were fabricated by coating a layer of the sensing material on homemade Al_2O_3 sensor substrates that were patterned with Au electrodes (Figure 4a). In our setup, the sensing conditions were maintained at a relative humidity of 90% to create an atmosphere similar to that of human breath. We found the optimum dopant concentrations of Pt, Rh, and Ir to be 0.04, 0.3, and 0.1 at% against tungsten oxide, respectively, in terms of the sensing performance. The optimal operating temperature was found to be at 350 °C in Pt-WO_3 and 400 °C in Rh-WO_3 and Ir-WO_3 NFs. Interestingly, the furnace-treated exsolved Pt-WO_3 NFs exhibited noticeable degradation of sensing performances after the first cycle of exposure and poor sensitivity (Figure S16), indicating that the oxide matrix compromised by harsh reductive treatment hinders their use as reliable chemiresistive

https://doi.org/10.1021/acsnano.2c05128
ACS Nano 2022, 16, 18133−18142

sensors. On the other hand, the IPL-MP treated M-WO_3 NFs showed an enhanced response (R_{air}/R_{gas}) upon exposure to H_2S compared to that of M-WO_3 NFs. Figure 4b–d exhibits enhanced sensing performances (i.e., selectivity, sensitivity, and durability) and a markedly stable response in repetitive exposures. IPL_exsolved M-WO_3 NFs exhibited noticeably high response (R_{air}/R_{gas} = 852.4, 19.2, 215.3) at 1 ppm of H_2S exposure, which is 7.9, 1.7, 2.8-fold higher than that of M-WO_3 NFs before IPL-MP treatment (Table S4). Interestingly, the Pt-WO_3 NFs at lower concentrations of H_2S (e.g., 100–1000 ppb concentrations), the differences in gas responses were even more significant. When 10 consecutive IPL-MP treatments were applied, the response greatly improved further to 63.8 at 100 ppb H_2S, which is 13.9-fold higher than that of Pt-WO_3 NFs (Figure S17). In addition to the excellent sensitivity, the IPL-treated WO_3 NFs with exsolved M NPs exhibited high selectivity toward H_2S against other interfering gases, including 1 ppm of NH_3, C_2H_5OH, C_3H_6O, and C_2H_6S (dimethylsulfide). In particular, the WO_3 NFs with exsolved Pt NPs prepared by IPL-MP treatments exhibit a selectivity (R_{H_2S}/R_{NH_3}) of 789.26 against NH_3, which is 8.77-fold higher compared to that of Pt-WO_3 NFs before IPL-MP treatment. These sensing trends were also consistent for WO_3 NFs decorated with exsolved Rh or Ir NPs as formed by IPL-MP treatment, both exhibiting improved H_2S sensing performances in terms of response and selectivity (Figure 4c,d). The IPL-treated WO_3 NFs decorated with exsolved Pt, Rh, and Ir NPs showed stable gas responses ($|R_{air}/R_{gas}|$ = 735.95, 15.4, 203.31 with a standard deviation of 36.35, 0.68, 11.61) across 235, 121, 121 cyclic exposures to 1 ppm of H_2S with no sign of decay in its high response values. We noted that the base resistance of the IPL-treated exsolved M-WO_3 NFs could be recovered with a reasonably fast rate upon removing H_2S from the environment, and the sensor responses show a linear trend from 800 to 200 ppb within the same experiment (Figure S18). Both of these observations indicate that the IPL-induced exsolved M NPs can adsorb and desorb H_2S molecules efficiently from their surface, unlike typical M NPs that form strong bindings to sulfur species that inhibit the adsorption of analytes on active sites.[33] The resistance to sulfur poisoning is a shared characteristic of exsolved metal NPs on ceramic supports, according to the previous literature,[34] and though the exact mechanism remains unclear, this nevertheless supports the fact that IPL successfully induces exsolution of M NPs even in an ambient environment. This is especially important for H_2S sensing applications since sulfur-based species are known to strongly interact with the surface of semiconducting metal oxides and catalytic metal NPs, which induces a poisoning effect that severely degrades the sensing performance especially upon repetitive operation for an extended periods.[35] Altogether, the IPL-treated M-WO_3 NFs serve as superior sensing materials for selective H_2S sensing, which can be attributed to the exsolution-induced chemical resilience against sulfur poisoning.

Furthermore, the specific socketing structures of exsolved metal NPs that strongly anchor them in the oxide lattice with reciprocal strain result in a robust structure with high sintering resistance. To investigate the structural resilience of the exsolved Pt NPs against repeated exposure to H_2S at high temperatures for long periods, we performed ex situ electron microscopy analysis and compared their morphology and composition before and after the 350 °C treatment for more than 40 h (Figure 4b). The HRTEM images of the IPL-treated WO_3 NFs decorated with exsolved Pt NPs after cyclic H_2S exposure revealed WO_3 (002) and Pt (111) lattice fringes with an interplanar distance of 3.87 and 2.2 Å, indicating no obvious structural changes to both the metal catalyst and the oxide support. The corresponding HAADF-STEM image, EDS elemental mapping, and line scan profile also confirm the exsolved Pt NPs exist even after hundreds of sensing cycles, maintaining a consistent size (≈3.5 nm) and distribution (Figure S19), which confirmed sintering resistance of the exsolved NPs. Altogether, we found that the IPL-treated WO_3 NFs decorated with exsolved metal NPs exhibit superior sensitivity toward H_2S due to their synergistic effect of heterojunctions (WO_3-WO_{3-x}) and spillover effects of the metal NPs as well as exceptional stability against sulfur poisoning.

CONCLUSION

In summary, we demonstrated that the IPL-MP treatment can induce the ultrafast exsolution of noble metal NPs (e.g., Pt, Rh, and Ir) from binary oxide hosts (i.e., WO_3) in ambient-air conditions. The rapid optical sintering (T > 1000 °C for 20 ms) process formed several heterojunctions in the host oxide as well as exsolved metallic (Pt, Rh, and Ir) NPs on the oxide NFs surface while causing minimal thermal degradation to the host oxide lattice, marking a notable improvement over conventional thermal processes. The resulting material exhibited unparalleled H_2S sensing performances due to the synergistic effect of exsolved metal NPs, which promote spillover effects, and heterojunctions in the host oxide, which facilitate electron transfer. Specifically, IPL-treated WO_3 NFs decorated with exsolved Pt NPs showed selectivity values that (R_{H_2S}/R_{NH_3}) surpassed 700 against common interfering gases, and their sensitivity values also remained stable for over 200 cycles of repeated exposure toward 1 ppm of H_2S gas. Altogether, IPL-derived ambient-air exsolution offers a versatile strategy for the preparation of robust and highly catalytic NPs with minimal damage to the host oxide for improving the practical viability of the exsolved catalysts.

METHODS

Materials. Ammonium metatungstate hydrate [$(NH_3)_6H_2W_{12}O_{40}\cdot_xH_2O$], PVP (Mw = 1,300,000 g mol^{-1}), chloroplatinic acid hexahydrate ($H_2PtCl_6\cdot 6H_2O$), rhodium chloride hydrate ($RhCl_3\cdot xH_2O$), iridium(III) chloride hydrate ($IrCl_3\cdot xH_2O$) were purchased from Sigma-Aldrich. Chemicals were used without purification.

Synthesis of IPL_Exsolved Noble Metal-WO_3 NFs. Ten mg of Pt-WO_3, Rh-WO_3, Ir-WO_3 NFs was dissolved in 500 μL of ethanol solvent and sonicated 1 min to disperse completely. The solution was drop-coated on a glass substrate using a micropipette (20 μL, 5 times) on the hot plate (60 °C). The radius of the samples was ≈0.5 cm on the glass substrate (Micro slide glass, 76 × 52 × 1.2 mm), and we prepared 8–10 samples on one substrate. The samples were fixed 4 cm away from the xenon lamp. The number of samples to irradiate at once was up to 40 due to the light from the xenon lamp was irradiated uniformly on a centimeter-scale (15 × 10 cm^2). The thickness of samples was optimized through the experiment with different thickness samples (Supporting Information for details, Figures S20–S22). In this method, the thickness of the WO_3 NFs was ≈30 μm, which was measured by a surface profiler (Tencor α-Step IQ) (Figure S20). By using this process, IPL_Pt-WO_3 NFs, IPL_Rh-WO_3 NFs, and IPL_Ir-WO_3 NFs were prepared, respectively. For the gas sensor application, the atomic percentages of Pt, Rh, and Ir about WO_3 were calculated to Pt (0.04), Rh (0.3), and Ir (0.1 at%).

https://doi.org/10.1021/acsnano.2c05128
ACS Nano 2022, 16, 18133–18142

Intense Pulsed Light Irradiation Process. The IPL system has five main components, including a simmer board, a xenon lamp, capacitors, a DC power supply, an insulated-gate bipolar transistor (IGBT), and an IR sensor system (Figure S23). The intensive pulsed light was irradiated by a xenon lamp, of which the wavelength spectrum ranges from 300 to 1000 nm (Figure S24). To turn on the xenon lamp, the simmer board ignites the xenon lamp to cause steamer breakdown. Next, the capacitors are charged until designated voltage (0−500 V) by DC power supply and then discharged by switching on the IGBT to induce arc breakdown to generate a flashlight, which induces the photothermal effects in materials. By adjusting the applied voltage, pulse on time, number of pulses, and distance between the lamp and samples, the light power density could be changed. The energy of intensive light was measured by laser power meters (NOVA II, Ophir). The tungsten oxide NFs coated on the glass substrate (Micro slide glass, 76 × 52 × 1.2 mm) were located 4 cm from the lamp. One shot and 10 shots of the flashlight irradiated samples for maximum energy densities (19.6−20 J cm^{-2}). The energy that is absorbed in materials was changed by various factors (e.g., photothermal conversion efficiency, light absorbance, defect). We calculated the absorbed energy of WO_3 NFs using xenon lamp spectrum and UV−vis diffuse reflectance spectra (Figures S24 and S25, Supporting Information for details).

An IR sensor system (CTlaser 3MH2, Optris) measured the elevated temperature during the IPL process. The IR sensor detects from 200 to 1500 °C; therefore, the base temperature is 200 °C. The sensors generated a red dot which read the temperature of the samples, and the samples were located at the proper distance to focus (15 cm). The measured analog signals are converted to digital signals by a data acquisition board (NI USB-6341 X series Multifunction DAQ, National Instruments). Since the temperature data were obtained with the emissivity value of the IR sensor at 1.00, these data were revised using tabulated values for the emissivity of tungsten oxide ($\varepsilon_{corrected}$ = 0.885).[36] The following equation was used for all samples to calculate the revised temperature data:

$$\frac{1}{T_{measured}} = \frac{1}{T_{corrected}} + \frac{\lambda \ln(\varepsilon_{measured}/\varepsilon_{corrected})}{C_2}$$

where the $T_{measured}$ is the raw data of samples, which $\varepsilon_{measured}$ is set at 1.00 by the IR sensor, $T_{corrected}$ is the temperature data that is corrected by considering emissivity of tungsten oxide, λ is the detection wavelength of IR sensor (2.3 μm), and C_2 is the second radiant constant (14388 μm K^{-1}).

Material Characterization. Transmission electron microscopy (TEM), scanning TEM images, and elemental analysis (e.g., line scan profile and mapping by energy-dispersive X-ray spectroscopy (EDS)) were conducted by Cs-corrected scanning transmission electron microscopy (STEM) (JEOL, JEM-ARM200F). The crystal structures were carried out powder X-ray diffractometer (PXRD) (Rigaku, D/MAX-RC 12 kW) using Cu Kα (λ = 1.54 Å) radiation. The lattice volumes of the crystal structure were calculated by using PDXL (Rigaku, ver2.8.4.0). The chemical elements and bonding states of W, O were analyzed using X-ray photoelectron spectroscopy (XPS) (Sigma Probe, Thermo VG Scientific) with Al Ka radiation (1486.7 eV).

Grain Size Measurement Using the Scherrer Equation. The crystalline sizes of WO_3 and M-WO_3 NFs before and after IPL-MP treatment were calculated using the Scherrer equation:

$$D = 0.9\lambda/\beta\cos(2\theta)$$

where D is the average grain size, λ is the wavelength of the X-ray radiation (0.154 nm for Cu Kα), and β is the full width at half-maximum of the diffraction peak at 2θ. For each sample, the grain sizes were computed with respect to the (200), (020), and (002) planes, and the arithmetic mean of the three values was reported as the average crystalline size.

Gas Sensing Measurements. First, the sensing materials, Pt-WO_3 NFs, IPL1_exsolved Pt-WO_3 NFs, IPL10_exsolved Pt-WO_3 NFs, Rh-WO_3 NFs, IPL_exsolved Rh-WO_3 NFs, and Ir-WO_3 NFs, IPL_exsolved Ir-WO_3 NFs, were coated on the Al_2O_3 substrate using the drop coating method. Each of the sensing materials were dispersed in ethanol (2 mg in 100 μL) then drop-coated using a micropipette (2.5 μL) several times on the hot plate (60 °C). The gas sensing tests were operated using a homemade gas sensing system consisting of a 16-channel multiplexer (34902A, Agilent), a data acquisition system (34972A, Agilent), which measured the resistance of 16 channels at 4 s intervals, and a mass flow control system control the concentration of exposed gases. The sensing measurements were operated in a highly humid atmosphere (90% RH), which is similar to human exhaled breath. The operating temperatures were controlled by applying a voltage to the Pt microheaters in the sensor substrate using a DC power supply (E3647A, Agilent). The operating temperatures were controlled by applying a voltage to the Pt microheaters in the sensor substrate using a DC power supply (E3647A, Agilent). The sensing measurements were operated in a highly humid atmosphere (90% RH), which is similar to human exhaled breath. The base resistances were stabilized in 2 h at setup temperature, and then, the sensitivity/selectivity/durability tests were conducted with 10/10/5 and 10 min on/off intervals with exposure to various gas and air repeatably. The change of resistance was converted into response (R_{air}/R_{gas}) which could denote the ratio between base resistance in air and resistance after gas exposure.

The sensor substrates have three main components: an alumina board, Au electrodes, and Pt heater. The size of alumina sensor substrates is 2.5 mm × 2.5 mm (thickness: 0.2 mm), and the substrates were printed with an interdigitated Au electrode (width: 25 μm, distance: 70 μm) on the front of the substrate and a Pt heater on the backside. The alumina substrate is connected to the four-pin systems with Pt wires. The connected two pins of electrodes measured resistance between electrodes and the other pins were connected to the Pt heater, which measured the operating temperature.

ASSOCIATED CONTENT

Supporting Information

The Supporting Information is available free of charge at https://pubs.acs.org/doi/10.1021/acsnano.2c05128.

EDS images, PXRD patterns, XPS data, SEM images, gas sensing performance results, TEM images, temperature−time graphs, UV−vis diffuse reflectance spectra, surface profiler graph, overall IPL system (PDF)

AUTHOR INFORMATION

Corresponding Authors

Il-Doo Kim − *Department of Materials Science and Engineering, Korea Advanced Institute of Science and Technology (KAIST), Yuseong-gu, Daejeon 34141, Republic of Korea; Membrane Innovation Center for Anti-Virus and Air-Quality Control, KAIST Institute for Nanocentury, Yuseong-gu, Daejeon 34141, Republic of Korea;* orcid.org/0000-0002-9970-2218; Email: idkim@kaist.ac.kr

Sung-Yool Choi − *School of Electrical Engineering and Center for Advanced Materials Discovery towards 3D Displays, Korea Advanced Institute of Science and Technology (KAIST), Yuseong-gu, Daejeon 34141, Republic of Korea;* orcid.org/0000-0002-0960-7146; Email: sungyool.choi@kaist.ac.kr

Authors

Euichul Shin − *Department of Materials Science and Engineering, Korea Advanced Institute of Science and Technology (KAIST), Yuseong-gu, Daejeon 34141, Republic of Korea; Membrane Innovation Center for Anti-Virus and*

Air-Quality Control, KAIST Institute for Nanocentury, Yuseong-gu, Daejeon 34141, Republic of Korea

Dong-Ha Kim − *Department of Materials Science and Engineering, Korea Advanced Institute of Science and Technology (KAIST), Yuseong-gu, Daejeon 34141, Republic of Korea; Membrane Innovation Center for Anti-Virus and Air-Quality Control, KAIST Institute for Nanocentury, Yuseong-gu, Daejeon 34141, Republic of Korea; Department of Chemistry, Massachusetts Institute of Technology, Cambridge, Massachusetts 02139, United States*

Jun-Hwe Cha − *School of Electrical Engineering and Center for Advanced Materials Discovery towards 3D Displays, Korea Advanced Institute of Science and Technology (KAIST), Yuseong-gu, Daejeon 34141, Republic of Korea*

Seolwon Yun − *School of Electrical Engineering and Center for Advanced Materials Discovery towards 3D Displays, Korea Advanced Institute of Science and Technology (KAIST), Yuseong-gu, Daejeon 34141, Republic of Korea*

Hamin Shin − *Department of Materials Science and Engineering, Korea Advanced Institute of Science and Technology (KAIST), Yuseong-gu, Daejeon 34141, Republic of Korea; Membrane Innovation Center for Anti-Virus and Air-Quality Control, KAIST Institute for Nanocentury, Yuseong-gu, Daejeon 34141, Republic of Korea*

Jaewan Ahn − *Department of Materials Science and Engineering, Korea Advanced Institute of Science and Technology (KAIST), Yuseong-gu, Daejeon 34141, Republic of Korea; Membrane Innovation Center for Anti-Virus and Air-Quality Control, KAIST Institute for Nanocentury, Yuseong-gu, Daejeon 34141, Republic of Korea;* orcid.org/0000-0002-0136-8427

Ji-Soo Jang − *Electronic Materials Center, Korea Institute of Science and Technology, Seoul 02792, Republic of Korea;* orcid.org/0000-0001-6018-7231

Jong Won Baek − *Department of Materials Science and Engineering, Korea Advanced Institute of Science and Technology (KAIST), Yuseong-gu, Daejeon 34141, Republic of Korea; Membrane Innovation Center for Anti-Virus and Air-Quality Control, KAIST Institute for Nanocentury, Yuseong-gu, Daejeon 34141, Republic of Korea*

Chungseong Park − *Department of Materials Science and Engineering, Korea Advanced Institute of Science and Technology (KAIST), Yuseong-gu, Daejeon 34141, Republic of Korea; Membrane Innovation Center for Anti-Virus and Air-Quality Control, KAIST Institute for Nanocentury, Yuseong-gu, Daejeon 34141, Republic of Korea*

Jaehyun Ko − *Department of Materials Science and Engineering, Korea Advanced Institute of Science and Technology (KAIST), Yuseong-gu, Daejeon 34141, Republic of Korea; Membrane Innovation Center for Anti-Virus and Air-Quality Control, KAIST Institute for Nanocentury, Yuseong-gu, Daejeon 34141, Republic of Korea*

Seyeon Park − *Department of Materials Science and Engineering, Korea Advanced Institute of Science and Technology (KAIST), Yuseong-gu, Daejeon 34141, Republic of Korea; Membrane Innovation Center for Anti-Virus and Air-Quality Control, KAIST Institute for Nanocentury, Yuseong-gu, Daejeon 34141, Republic of Korea*

Complete contact information is available at: https://pubs.acs.org/10.1021/acsnano.2c05128

Notes

The authors declare no competing financial interest.

ACKNOWLEDGMENTS

This work was supported by Samsung Research Funding and Incubation Center of Samsung Electronics under project number SRFC-MA1502-52. This work was also supported by the National Research Foundation of Korea (NRF) grant of the Korean Government (NRF2017M3D9A107350122).

REFERENCES

(1) Wang, C.; Ciganda, R.; Salmon, L.; Gregurec, D.; Irigoyen, J.; Moya, S.; Ruiz, J.; Astruc, D. Highly Efficient Transition Metal Nanoparticle Catalysts in Aqueous Solutions. *Angew. Chem.* **2016**, *128* (9), 3143−3147.

(2) Zheng, N.; Stucky, G. D. A General Synthetic Strategy for Oxide-Supported Metal Nanoparticle Catalysts. *J. Am. Chem. Soc.* **2006**, *128* (44), 14278−14280.

(3) Kim, J. H.; Kim, J. K.; Liu, J.; Curcio, A.; Jang, J. S.; Kim, I. D.; Ciucci, F.; Jung, W. C. Nanoparticle Ex-Solution for Supported Catalysts: Materials Design, Mechanism and Future Perspectives. *ACS Nano* **2021**, *15* (1), 81−110.

(4) Yu, S.; Yoon, D.; Lee, Y.; Yoon, H.; Han, H.; Kim, N.; Kim, C. J.; Ihm, K.; Oh, T. S.; Son, J. Metal Nanoparticle Exsolution on a Perovskite Stannate Support with High Electrical Conductivity. *Nano Lett.* **2020**, *20* (5), 3538−3544.

(5) Jo, Y. R.; Koo, B.; Seo, M. J.; Kim, J. K.; Lee, S.; Kim, K.; Han, J. W.; Jung, W. C.; Kim, B. J. Growth Kinetics of Individual Co Particles Ex-Solved on $SrTi_{0.75}Co_{0.25}O_{3-}$ Polycrystalline Perovskite Thin Films. *J. Am. Chem. Soc.* **2019**, *141* (16), 6690−6697.

(6) Li, X.; Dai, L.; He, Z.; Meng, W.; Li, Y.; Wang, L. In Situ Exsolution of PdO Nanoparticles from Non-Stoichiometric $LaFeP-d_{0.05}O_{3+\Delta}$ Electrode for Impedancemetric NO_2 Sensor. *Sensors Actuators, B Chem.* **2019**, *298*, 126827.

(7) Gao, Y.; Chen, D.; Saccoccio, M.; Lu, Z.; Ciucci, F. From Material Design to Mechanism Study: Nanoscale Ni Exsolution on a Highly Active A-Site Deficient Anode Material for Solid Oxide Fuel Cells. *Nano Energy* **2016**, *27*, 499−508.

(8) Myung, J. H.; Neagu, D.; Miller, D. N.; Irvine, J. T. S. Switching on Electrocatalytic Activity in Solid Oxide Cells. *Nature* **2016**, *537* (7621), 528−531.

(9) Tan, J.; Lee, D.; Ahn, J.; Kim, B.; Kim, J.; Moon, J. Thermally Driven in Situ Exsolution of Ni Nanoparticles from $(Ni, Gd)CeO_2$ for High-Performance Solid Oxide Fuel Cells. *J. Mater. Chem. A* **2018**, *6* (37), 18133−18142.

(10) Jang, J. S.; Kim, J. K.; Kim, K.; Jung, W. G.; Lim, C.; Kim, S.; Kim, D. H.; Kim, B. J.; Han, J. W.; Jung, W. C.; Kim, I. D. Dopant-Driven Positive Reinforcement in Ex-Solution Process: New Strategy to Develop Highly Capable and Durable Catalytic Materials. *Adv. Mater.* **2020**, *32* (46), 2003983.

(11) Yao, Y.; Huang, Z.; Xie, P.; Lacey, S. D.; Jacob, R. J.; Xie, H.; Chen, F.; Nie, A.; Pu, T.; Rehwoldt, M.; Yu, D.; Zachariah, M. R.; Wang, C.; Shahbazian-Yassar, R.; Li, J.; Hu, L. Carbothermal Shock Synthesis of High-Entropy-Alloy Nanoparticles. *Science (80-.).* **2018**, *359* (6383), 1489−1494.

(12) Fuku, K.; Hayashi, R.; Takakura, S.; Kamegawa, T.; Mori, K.; Yamashita, H. The Synthesis of Size- and Color-Controlled Silver Nanoparticles by Using Microwave Heating and Their Enhanced Catalytic Activity by Localized Surface Plasmon Resonance. *Angew. Chem.* **2013**, *125* (29), 7594−7598.

(13) Park, S.; Park, J.; Kim, Y.-g.; Bae, S.; Kim, T.-W.; Park, K.-I.; Hong, B. H.; Jeong, C. K.; Lee, S.-K. Laser-Directed Synthesis of Strain-Induced Crumpled MoS_2 Structure for Enhanced Tribo-electrification toward Haptic Sensors. *Nano Energy* **2020**, *78*, 105266.

(14) Im, T. H.; Lee, J. H.; Wang, H. S.; Sung, S. H.; Kim, Y. B.; Rho, Y.; Grigoropoulos, C. P.; Park, J. H.; Lee, K. J. Flashlight-Material Interaction for Wearable and Flexible Electronics. *Mater. Today* **2021**, *51*, 525−551.

(15) Kim, D.-H.; Cha, J.-H.; Shim, G.; Kim, Y. H.; Jang, J.-S.; Shin, H.; Ahn, J.; Choi, S.-Y.; Kim, I.-D. Flash-Thermochemical Engineering of Phase and Surface Activity on Metal Oxides. *Chem.* **2022**, *8*, 1014−1033.
(16) Cha, J. H.; Kim, D. H.; Park, C.; Choi, S. J.; Jang, J. S.; Yang, S. Y.; Kim, I. D.; Choi, S. Y. Low-Thermal-Budget Doping of 2D Materials in Ambient Air Exemplified by Synthesis of Boron-Doped Reduced Graphene Oxide. *Adv. Sci.* **2020**, *7* (7), 1903318.
(17) Pascariu, P.; Homocianu, M.; Cojocaru, C.; Samoila, P.; Airinei, A.; Suchea, M. Preparation of La Doped ZnO Ceramic Nanostructures by Electrospinning-Calcination Method: Effect of La^{3+} Doping on Optical and Photocatalytic Properties. *Appl. Surf. Sci.* **2019**, *476*, 16−27.
(18) Desilvestro, J.; Neumann-Spallart, M. Photoredox Reactions on Semiconductors at Open Circuit. Reduction of Fe^{3+} on WO_3 Electrodes and Particle Suspensions. *J. Phys. Chem.* **1985**, *89* (17), 3684−3689.
(19) Zheng, H.; Ou, J. Z.; Strano, M. S.; Kaner, R. B.; Mitchell, A.; Kalantar-Zadeh, K. Nanostructured Tungsten Oxide - Properties, Synthesis, and Applications. *Adv. Funct. Mater.* **2011**, *21* (12), 2175−2196.
(20) Obeid, M. M.; Jappor, H. R.; Al-Marzoki, K.; Al-Hydary, I. A.; Edrees, S. J.; Shukur, M. M. Unraveling the Effect of Gd Doping on the Structural, Optical, and Magnetic Properties of ZnO Based Diluted Magnetic Semiconductor Nanorods. *RSC Adv.* **2019**, *9* (57), 33207−33221.
(21) Rahimnejad, S.; He, J. H.; Pan, F.; Lee, X.; Chen, W.; Wu, K.; Xu, G. Q. Enhancement of the Photocatalytic Efficiency of WO_3 Nanoparticles via Hydrogen Plasma Treatment. *Mater. Res. Express* **2014**, *1* (4), 045044.
(22) Wu, H.; Xu, M.; Da, P.; Li, W.; Jia, D.; Zheng, G. WO_3-Reduced Graphene Oxide Composites with Enhanced Charge Transfer for Photoelectrochemical Conversion. *Phys. Chem. Chem. Phys.* **2013**, *15* (38), 16138−16142.
(23) Briggs, D. X-Ray Photoelectron Spectroscopy (XPS). *Handb. Adhes. Second Ed.* **2005**, 621−622.
(24) Köferstein, R.; Jäger, L.; Ebbinghaus, S. G. Magnetic and Optical Investigations on $LaFeO_3$ Powders with Different Particle Sizes and Corresponding Ceramics. *Solid State Ionics* **2013**, *249*−*250*, 1−5.
(25) Wu, X.; Yu, Y.; Chen, Y.; Li, L.; Ma, Z. F.; Yin, Y. M. Construction of Multifunctional Nanoarchitectures in One Step on a Composite Fuel Catalyst through in Situ Exsolution of $La_{0.5}Sr_{0.5}Fe_{0.8}Ni_{0.1}Nb_{0.1}O_3$. *ACS Appl. Mater. Interfaces* **2020**, *12* (31), 34890−34900.
(26) Lv, H.; Liu, T.; Zhang, X.; Song, Y.; Matsumoto, H.; Ta, N.; Zeng, C.; Wang, G.; Bao, X. Atomic-Scale Insight into Exsolution of CoFe Alloy Nanoparticles in $La_{0.4}Sr_{0.6}Co_{0.2}Fe_{0.7}Mo_{0.1}O_{3-\delta}$ with Efficient CO_2 Electrolysis. *Angew. Chemie - Int. Ed.* **2020**, *59* (37), 15968−15973.
(27) Opitz, A. K.; Nenning, A.; Vonk, V.; Volkov, S.; Bertram, F.; Summerer, H.; Schwarz, S.; Steiger-Thirsfeld, A.; Bernardi, J.; Stierle, A.; Fleig, J. Understanding Electrochemical Switchability of Perovskite-Type Exsolution Catalysts. *Nat. Commun.* **2020**, *11* (1), 1−10.
(28) Shin, H.; Kim, D. H.; Jung, W.; Jang, J. S.; Kim, Y. H.; Lee, Y.; Chang, K.; Lee, J.; Park, J.; Namkoong, K.; Kim, I. D. Surface Activity-Tuned Metal Oxide Chemiresistor: Toward Direct and Quantitative Halitosis Diagnosis. *ACS Nano* **2021**, *15* (9), 14207−14217.
(29) Jha, R. K.; D'Costa, J. V.; Sakhuja, N.; Bhat, N. $MoSe_2$ Nanoflakes Based Chemiresistive Sensors for Ppb-Level Hydrogen Sulfide Gas Detection. *Sensors Actuators, B Chem.* **2019**, *297*, 126687.
(30) Choi, S. J.; Jang, B. H.; Lee, S. J.; Min, B. K.; Rothschild, A.; Kim, I. D. Selective Detection of Acetone and Hydrogen Sulfide for the Diagnosis of Diabetes and Halitosis Using SnO_2 Nanofibers Functionalized with Reduced Graphene Oxide Nanosheets. *ACS Appl. Mater. Interfaces* **2014**, *6* (4), 2588−2597.
(31) Mews, M.; Korte, L.; Rech, B. Oxygen Vacancies in Tungsten Oxide and Their Influence on Tungsten Oxide/Silicon Heterojunction Solar Cells. *Sol. Energy Mater. Sol. Cells* **2016**, *158*, 77−83.
(32) Ling, Z.; Leach, C. The Effect of Relative Humidity on the NO_2 Sensitivity of a SnO_2/WO_3 Heterojunction Gas Sensor. *Sensors Actuators, B Chem.* **2004**, *102* (1), 102−106.
(33) Zhou, N.; Yin, Y.-M.; Chen, Z.; Song, Y.; Yin, J.; Zhou, D.; Ma, Z.-F. A Regenerative Coking and Sulfur Resistant Composite Anode with Cu Exsolution for Intermediate Temperature Solid Oxide Fuel Cells. *J. Electrochem. Soc.* **2018**, *165* (9), F629−F634.
(34) Papaioannou, E. I.; Neagu, D.; Ramli, W. K. W.; Irvine, J. T. S.; Metcalfe, I. S. Sulfur-Tolerant, Exsolved Fe-Ni Alloy Nanoparticles for CO Oxidation. *Top. Catal.* **2019**, *62* (17−20), 1149−1156.
(35) Kato, S.; Hirano, Y.; Iwata, M.; Sano, T.; Takeuchi, K.; Matsuzawa, S. Photocatalytic Degradation of Gaseous Sulfur Compounds by Silver-Deposited Titanium Dioxide. *Appl. Catal. B Environ.* **2005**, *57* (2), 109−115.
(36) Bu, X.; Zhou, Y.; He, M.; Chen, Z.; Zhang, T.; Wang, Y. Fabrication and Characterization of Optically Active Polyacetylene@WO_3 Nanorodhybrids with Low Infrared Emissivity. *Mater. Lett.* **2014**, *120*, 239−242.

https://doi.org/10.1021/acsnano.2c05128
ACS Nano 2022, 16, 18133−18142